HHS Public Access

Author manuscript

IEEE Trans Biomed Eng. Author manuscript; available in PMC 2023 June 01.

Published in final edited form as:

IEEE Trans Biomed Eng. 2022 June ; 69(6): 1909–1919. doi:10.1109/TBME.2021.3130540.

Towards Estimation of Tidal Volume and Respiratory Timings via Wearable-Patch-Based Impedance Pneumography in Ambulatory Settings

John A. Berkebile [Student Member, IEEE],
School of Electrical and Computer Engineering, Georgia Institute of Technology, Atlanta, GA 30308 USA

Samer A. Mabrouk,
School of Electrical and Computer Engineering, Georgia Institute of Technology, Atlanta, GA 30308 USA

Venu G. Ganti [Student Member, IEEE],
Bioengineering Graduate Program, Georgia Institute of Technology

Adith V. Srivatsa,
Wallace H. Coulter Department of Biomedical Engineering, Georgia Institute of Technology

Jesus A. Sanchez-Perez,
School of Electrical and Computer Engineering, Georgia Institute of Technology, Atlanta, GA 30308 USA

Omer T. Inan [Senior Member, IEEE]
School of Electrical and Computer Engineering, Georgia Institute of Technology, Atlanta, GA 30332 USA; Wallace H. Coulter Department of Biomedical Engineering, Georgia Institute of Technology, Atlanta, GA 30332 USA

Abstract

Objective: Evaluating convenient, wearable multi-frequency impedance pneumography (IP) based respiratory monitoring in ambulatory persons with novel electrode positioning.

Methods: A wearable multi-frequency IP system was utilized to estimate tidal volume (TV) and respiratory timings in 14 healthy subjects. A 5.1 cm × 5.1 cm tetrapolar electrode array, affixed to the sternum, and a conventional thoracic electrode configuration were employed to measure the respective IP signals, patch and thoracic IP. Data collected during static postures—sitting and supine—and activities—walking and stair-stepping—were evaluated against a simultaneously-obtained spirometer (SP) volume signal.

Resuls: Across all measurements, estimated TV obtained from the patch and thoracic IP maintained a Pearson correlation coefficient (r) of 0.93±0.05 and 0.95±0.05 to the ground truth TV, respectively, with an associated root-mean-square error (RMSE) of 0.177 L and 0.129 L,

Corresponding author: John A. Berkebile. jaberkebile@gatech.edu.

respectively. Average respiration rates (RRs) were extracted from 30-second segments with mean-absolute-percentage errors (MAPEs) of 0.93% and 0.74% for patch and thoracic IP, respectively. Likewise, average inspiratory and expiratory timings were identified with MAPEs less than 6% and 4.5% for patch and thoracic IP, respectively.

Conclusion: We demonstrated that patch IP performs comparably to traditional, cumbersome IP configurations. We also present for the first time, to the best of our knowledge, that IP can robustly estimate breath-by-breath TV and respiratory timings during ambulation.

Significance: This work represents a notable step towards pervasive wearable ambulatory respiratory monitoring via the fusion of a compact chest-worn form factor and multi-frequency IP that can be readily adapted for holistic cardiopulmonary monitoring.

Keywords

impedance pneumography; respiratory monitoring; wearable sensing

I. Introduction

RESPIRATORY monitoring is critical for providing valuable cardiopulmonary health markers such as tidal volume (TV), the volume of air inhaled and exhaled by the lungs during a single breath, and respiratory rate (RR), the number of breaths per minute (brpm). Such parameters become altered in a diseased state such as heart failure (HF) [1], [2] or chronic obstructive pulmonary disease (COPD) [3] and therefore are important to monitor. Similarly, respiratory phase timings, including inspiratory (INT) and expiratory (EXT) times, contain physiological information that can be leveraged in the assessment of sleep-related breathing disorders, such as the classification of various hypopneas [4], and facilitate the quantification of the body's response to stress and neuromodulation [5]. Methods that enable the accurate, routine monitoring of these salient respiratory parameters are essential for quantifying exacerbations in pulmonary status.

However, despite the overwhelming need for reliable at-home monitoring underscored by the recent global COVID-19 pandemic [6], conventional techniques for extracting these parameters are still restrained to clinical sites and are virtually nonexistent in ambulatory settings [7]. Additionally, these vital respiratory parameters—if even monitored—are commonly evaluated subjectively and infrequently, and are constrained to static environments, further hindering their clinical impact [8]. For instance, RR remains a vital sign often recorded manually [9], which has contributed to its neglect in hospital settings [10], whereas traditional TV monitoring approaches, such as spirometry or capnography, require intrusive masks or mouthpieces that can prompt undesirable alterations in respiratory patterns [11]. This has culminated in a scarcity of TV monitoring due to the lack of capable, unobtrusive technologies [7]. Thus, the development of noninvasive, continuous monitoring alternatives suitable for ambulatory tracking of pulmonary function is necessary.

Impedance pneumography (IP) has long been considered a potential replacement for traditional respiratory monitoring methods as it offers a less intrusive technique for acquiring TV and respiratory timings on a breath-by-breath basis. IP is a measure of

the variations in electrical bioimpedance (EBI) of the thoracic cavity. EBI, the electrical conductivity of tissue measured by distributing an alternating current through distally placed electrodes to a segment of the body and recording the voltage drop with proximal electrodes, has been shown to correlate with the air content of the lungs during breathing [12], [13]. The tissue impedance being measured is dictated by the electrode placement which, when configured for IP, commonly encapsulates both sides of the thorax to direct the current through the lungs, with varying configurations previously employed [14].

However, several limitations have prevented the widespread implementation of IP, as the distance between electrodes complicates the adoption of a wearable form factor, and the skin-electrode interfaces inherently introduce motion artifacts which are detrimental to the signal quality [15], [16]. Classic electrode configurations require electrode leads that obtrusively span across the body, to encompass the entire thoracic cavity for high signal quality, negating the potential for a compact form factor when using IP. Previous works have emphasized reducing the inter-electrode distances, yet the systems either utilized a 2-electrode EBI system that does not mitigate the skin-electrode impedance as the 4-electrode configuration does [17], [18], or exhibited insufficient volume estimation accuracy for practical use in the limited settings that were tested [19]. Efforts have also been made to alleviate the issue of motion artifacts [20]–[22], but IP has thus far been relegated to predominantly static applications. While RR has previously been estimated from IP during active measurements [23], [24], the efficacy of active TV estimation has never been explicitly demonstrated. In the previous studies using IP-derived volume in active conditions, only minute ventilation (MV), the product of TV and RR, was reported for measurements acquired while cycling [24] and running [25]. Specifically, these studies provided no TV-specific metrics but indicated that both MV and RR estimation during cycling were unsatisfactory and that, during running, inaccurate TV estimation produced inconsistent results across subjects. Due to the confines of these studies, e.g., the limited subject demographic, lack of breath-by-breath analysis, and the indeterminate results, the feasibility of ambulatory IP-based respiratory monitoring is not yet conclusive. These unresolved areas have hindered IP's clinical usefulness for tracking the progression of diseases with respiratory complications, such as HF and COPD which are routinely assessed through cardiopulmonary exercise testing [26], [27], where ambulatory monitoring is a prerequisite.

To address these challenges, we first introduced a novel, small form factor IP electrode configuration for improved convenience prior to demonstrating, for the first time, accurate estimation of TV, RR, and respiratory phase timings in both active and static scenarios. Finally, we present a multi-frequency IP technique that accounts for confounding variations between subjects that would otherwise preclude cardiorespiratory sensing. This multifaceted IP-based respiratory monitoring approach is depicted in Fig. 1.

II. System Overview and Methods

A. Impedance Pneumography System

The wearable hardware previously used by our group for bioimpedance spectroscopy [28] was modified to allow for continuous measuring of impedance pneumography (IP),

defined in this work as the real (resistive) component of EBI—which has exhibited strong correlations to lung volume [29]. The printed circuit board responsible for measuring EBI was revised to include the AD5940 integrated circuit (Analog Devices, Cambridge, MA), an improved version of the previous EBI front end, but the rest of the overall architecture remained similar. This new integrated circuit supports the four-electrode configuration by default and has an increased frequency range (up to 200 kHz) with milliohm resolution that is apt for measuring thoracic EBI at the desired frequencies.

A controlled alternating voltage of 450 mV is generated by the AD5940 to excite the body, with current-limiting resistors to ensure that the IEC 60601-1-11 safety guidelines on injected current are met [30]. Each EBI measurement returns complex current and voltage values, corresponding to the tissue that the current flows through, which are saved onto an SD card for later retrieval. These values can be converted into real and imaginary impedance components by calibrating using the method in [31]. Specific firmware was written to cyclically generate the excitation signals and measure EBI across the conventional IP frequency range at four discrete frequencies: 5 kHz, 50 kHz, 100 kHz, and 150 kHz [32]. An EBI measurement sweep of all four excitation frequencies requires 62.5 ms, resulting in a sampling rate of 16 Hz for each continuous IP signal. The frequency of the excitation signal influences the current path; high frequencies propagate through intracellular pathways and low frequencies through extracellular paths, resulting in each frequency detecting differing degrees of lung content and motion artifacts [32]. The motivation for measuring IP at multiple frequencies was twofold: (1) identify frequencies that are less susceptible to the anatomical variations of the thorax from subject to subject; and (2) elucidate how multiple excitation frequencies can contribute to robust signal quality in anticipation of motion artifacts.

The device housing was previously adapted to be worn on the arm for uninhibited access to the thorax and chest [33]. The EBI electrodes, representing the current source ($I+$) and sink ($I-$) and the positive ($V+$) and negative ($V-$) voltage references, were placed in two configurations during this study: (1) the proposed configuration (patch IP) and (2) the conventional configuration (thoracic IP). The patch IP electrodes were located directly underneath the sternoclavicular joint over the manubrium, centered on the midsternal line, embedded in a custom 3D printed square patch with the current electrodes placed superior to the voltage electrodes. The distance between the center of each electrode in the patch, which also helped reduce electrode slippage [16], was 5.1 cm, with the positive electrodes for each pair placed on the left side of the chest as shown in Fig. 2. The vertically oriented current and voltage electrode pairs and sternum positioning were utilized as in previous works [18], [19], [22], where similar orientation and placement were employed, but with greater inter-electrode distances. The proximal location enables the excitation currents to penetrate both lungs, which is vital for obtaining sufficient signal quality due to the shortening of the current paths because of the electrode proximity. The thoracic IP configuration spanned across the thorax with the voltage electrodes positioned at the intersections of the midaxillary and 5^{th} intercostal line and the current electrodes placed on the underarms, equidistant from the armpit relative to the voltage electrodes. This configuration was selected from literature for its high linearity between measured IP and lung volume, and to exemplify other typical transthoracic electrode arrays [14].

B. Data Collection

The experimental data was acquired under a Georgia Institute of Technology Institutional Review Board (H18452) approved protocol. This study was conducted with 14 (8 males, 6 females) young, healthy subjects (Age: 24.6 ± 2.3 years; Height: 172.1 ± 14.0 cm; Weight: 67.8 ± 16.1 kg) with no record of cardiopulmonary disease. Simultaneous measurements from the previously detailed IP system and the Biopac TSD117A spirometry module (Biopac Systems, Goleta, CA, USA), acquired at a sampling rate of 2 kHz from the Biopac MP150 data acquisition system, were collected during controlled breathing tasks. A nose clip, to direct airflow through the spirometer only, and a disposable mouthpiece, to prevent infection, were used. The spirometer (SP) flow signal was checked prior to each measurement to ensure that no baseline drift had occurred. Fig. 2 summarizes the experimental setup.

For both electrode configurations, subjects were asked to modulate their breathing volume while maintaining two static postures and performing two activities: sitting, lying supine, walking, and stair-stepping, respectively. The protocol duration was 6 minutes for the static measurements and 5 minutes for the active. The walking measurement was performed on a treadmill at a set speed of 2 miles per hour (mph). The stair-stepping task used a platform on which subjects were instructed to step up onto and then step backwards, down onto the floor, completing this routine 24 times per minute at a controlled rate. We selected these active scenarios to function both as a surrogate for real-world operating conditions and as distinct sources of motion artifacts, where walking induces homogeneous distortions onto the IP data while stair-stepping generates more periodic and perturbative artifacts.

The protocol, detailed in Fig. 2, contained three distinct periods of breath modulation consisting of baseline breathing (60 seconds), shallow breathing (120 seconds), and deep breathing (120 seconds). The baseline portion served as the reference TV from which the subjects were asked to deliberately decrease or increase for the shallow and deep sections, respectively. Specific breathing depths were not enforced, thus lung volumes varied naturally between subjects. The static measurements included additional rests to allow subjects to recover, whereas the active measurements, to emulate realistic activity more closely, transitioned directly between the different breathing levels. The breathing rate was dictated by a metronome, with the static measurements having an RR of 12 brpm and the active measurements an RR of 24 brpm. These parameters were selected to assess the system at expected RRs within ambulatory conditions. A controlled breathing rate allowed the effects of ambulation on the respiratory signal to be isolated, as opposed to the entangling of natural respiratory variability with externally induced artifacts.

C. Signal Processing

The raw SP signal and multi-frequency IP signals were processed prior to extracting volume and respiratory timings, as illustrated in Fig. 3. All signal processing was completed in MATLAB (R2020b, Natick, MA). Initially, all signals were linearly resampled, utilizing an antialiasing filter, to 100 Hz for uniformity. The signals were then aligned by computing the lag at the maximum cross-correlation value between the derivative of the IP signal—a surrogate for the flow [13]—and the SP flow signal. The aligned IP volume and SP flow

signals were conditioned with 10^{th}-order finite impulse response (FIR) filters using Kaiser window: a low-pass with 1 Hz cutoff for the SP signal and a bandpass with a passband of 0.1-1 Hz for the IP signal. This approach eliminates unwanted cardiac components and high frequency noise, while also extricating the IP signals from low frequency baseline drift. In addition, a Savitzky-Golay (S-G) smoothing filter, with a 1000 ms frame size and second-order fitting, was applied to the IP to attenuate cardiogenic oscillations, as detailed in [13]. To convert the respiratory flow signal acquired from the SP into a groundtruth volume signal suitable for direct comparison against the IP surrogate, each breath—partitioned by successive zero-crossing points that indicate the onset of inspiration or expiration—was integrated via the approach in [29]. To prevent the detection of zero-crossing points that were not indicative of respiratory phase transitions, but of breathing irregularities, a minimum separation of 1.5 s was enforced, translating to a maximum breathing rate of 40 brpm.

After separating these preprocessed volume signals into 30-second segments, resulting in 10 segments per measurement, the local extrema containing the salient respiratory timing and TV information were detected breath-by-breath. The expiration and inspiration onsets, subsequently referred to as the peaks and valleys respectively, of the SP signal were found by projecting the zero-crossing points of the flow signal onto the volume signal, which corresponded to the maximum and minimum volume of each breath. For the IP signal, each segment was first linearly detrended to eliminate any residual drift that is common in respiratory signals. The criteria for valid peaks within a segment comprised of a minimum peak prominence of half of the segment's variance and a minimum peak separation of 1.5 s, as with the SP signal. With all peak locations in a segment detected, the indices of the valleys were then designated as the index of the minimum value within the inter-breath intervals (IBIs), the region between consecutive peaks. Finally, the extrema indices were mapped onto the IP signal prior to detrending to obtain the true peak and valley amplitudes to avoid potential amplitude distortion from detrending.

Due to breath-to-breath variability in morphology and the presence of artifacts, a signal quality index (SQI) was computed for each 30-second segment to ensure that only representative breaths were preserved. A simplified version of the SQI from [34] was employed in addition to the aforementioned physiologically-informed restraints enforced on breath detection. A breath template was formed by averaging all detected breaths within the 30-second segment. The individual breaths were correlated against this aggregated breath template, and segments were deemed high quality if the resulting mean correlation for the entire segment was above 0.7, which was lowered from the 0.75 value used in previous work to guarantee that—in the intentionally noisy scenarios—enough segments were suitable for feature extraction. This threshold proved sufficient for identifying the key signal landmarks during feature extraction, as presented in the results section.

The respiratory features, namely TV, RR, and phase timings, were computed in this work by utilizing the amplitude and location of the peaks and valleys of the volume signals, as in [35]. The peak-to-peak values derived from each breath serve as the ground truth TV from the integrated SP signal, and as the correlative TV estimation feature from the IP signals, producing comparable breath-by-breath TV features. An average RR for a segment was

obtained by averaging the instantaneous RRs, calculated by multiplying the reciprocal of the IBIs (in seconds) by 60. Respiratory phase timings, INT and EXT, were likewise averaged over an entire segment and were evaluated as the time difference between the first peak and valley and between the valley and second peak, respectively. Averaging was employed for the time-based features as natural variability between instantaneous breath timings can skew results if examined individually.

D. Calibration Method

As the linear relationship between IP and TV has been demonstrated to vary among differing postures, calibration coefficients (CCs) are often posture-specific, in addition to subject-specific [36]. No standardized calibration methodology for estimating TV from IP exists, but it is desirable to ease the burden of calibration by reducing the number of breaths required for satisfactory calibration. Thus, to convert IP peak-to-peak amplitude to TV, calibration points were allocated from three of the ten 30-second segments, one for each of the three breathing tasks. The segment in each breathing category with the highest SQI was chosen for calibration, to ensure indicative breaths were included. All but one measurement retained at least six high quality segments after processing, with a single measurement having only five quality segments—two of which were used for calibration. Therefore, the calibration set was always less than 50% of the entire measurement and typically included only 30% of all data points.

Applying these calibration sets, multiple linear regressions were carried out to produce CCs comprising of the slope and y-intercept of the best fit line. The remaining data points were mapped to a TV estimate along the regressed line. Each of the four IP signals were calibrated individually, as the IP peak-to-peak amplitudes differ—which impacts the CCs—with frequency, and variations in SQI among the IP frequencies caused the selected calibration segments to occasionally differ between the IP signals. Such calibration has been shown to remain effective for several days without significant loss of accuracy [36], which we validated by acquiring additional measurements an average of 15 days after the initial measurement for a subset of the subjects (n=4). This produced six pairs of comparable datasets with subjects in similar postures and using the same electrode configuration for direct assessment. The longevity of IP calibration was evaluated by using the CCs derived from the initial measurement, applying them on the corresponding follow-up data, and comparing the performance. To assess the differences in CCs between the patch and thoracic IP as well as intra-subject variability, we statistically analyzed the CCs produced by the patch and thoracic configurations across all subjects and activities. The outcomes of these analyses are reported in the results section.

E. Statistical Analysis

Among the 14 subjects, a single subject (Subject 13) was removed from the final analysis due to an unacceptably low number of high-quality segments being retained after the SQI, with only 55% of all segments retained for the best performing IP frequency with the patch configuration. This subject suffered a prior clavicular injury near to the electrode placement which likely impacted the penetration depth of the excitation currents, a theory reinforced by the subject’s average peak-to-peak impedance change being the lowest across all subjects.

For the analyzed data, outliers were classified for both TV and respiratory timings. TV regression outliers, categorized as estimated values that produced a residual larger than anticipated in 95% of future observations, were removed from analysis. RR, INT, and EXT values were regarded as outliers if more than three scaled median absolute deviations (MAD) away from the median of a measurement. Pearson's correlation coefficient (r) was calculated to demonstrate the relationship between IP estimated and true TV. The root-mean-square error (RMSE), a measure sensitive to large errors that are important in diagnostic devices, was computed as the root-mean-square of the difference between the ground truth and estimated TV, and the mean-absolute error (MAE) was calculated as the absolute difference between estimated and true RR. To account for variability across the measurements, the mean-absolute-percentage error (MAPE) was also calculated for all parameters. Mean error (ME) was computed to determine the bias of the estimations. Bland-Altman analysis with 95% limits of agreement was conducted for TV and RR estimation to depict the agreement between the estimated and reference values.

All metrics were derived for each measurement, and subject averages were determined for both electrode configurations. Two-sample t-tests (two-tailed) were utilized to determine the statistical significance ($p<0.05$) of the differences in RMSE and MAPE between the electrode configurations, as well as differences between the generated CCs.

III. Results

Due to the aggregated results for each IP frequency producing similar estimation accuracy for both the patch and thoracic IP, with TV performance specifically summarized in Table 1, only the excitation frequencies with the greatest number of quality segments were included in the following figures and Table 2. The 50 kHz patch data consisted of 90% of all recorded 30-second segments and the 100 kHz thoracic data included data from 96% of segments. Therefore, the following patch IP and thoracic IP results depict the performance of the 50 kHz and 100 kHz IP signals, respectively, unless otherwise mentioned. Each individual subject retained at least 78% of segments for the patch IP, and 85% for the thoracic IP across both configurations and testing environments.

The measurement-specific and aggregated results across all tested scenarios for both configurations are summarized in Table 2.

A. Tidal Volume Estimation

Fig. 4(a) depicts the relationship between the patch IP peak-to-peak impedance changes and the reference TV for each posture and activity. The subject-specific plots highlight the wide dynamic range, from less than 100 mL up to 5 L, that TV was estimated across, and the significant physiological diversity observed among the subjects. The average coefficient of determination (R^2) and RMSE, calculated after calibrating each measurement using the best fit line as shown in the plots, across the four measurements were reported per subject. Strong correlations were observed across all subjects with average R^2 values of 0.880 and 0.913 for the patch IP and thoracic IP, respectively.

Fig. 4(b) illustrates the correlation plots for the patch IP estimated TV across all subjects, divided to explicitly show static—which can be compared against previous work—and the state-of-the-art active results. The patch IP MAPE values were 12.97% and 16.90% for the static and active measurements, all four scenarios for these select frequencies. Table 1 explicitly details the percentage of segments used for all subjects for respectively. The incongruity in the number of points for the static and active measurements is due to the active experiments dictating an RR twice that of the static measurements, greatly increasing the number of breaths detected and therefore the number of TV estimations.

Fig. 4(c) displays the Bland-Altman plots of the estimated and true TV for the two classes of measurements. The static measurements had confidence intervals of 0.378 L and 0.296 L, whereas the active measurements showed expanded thresholds of 0.418 L and 0.342 L for the patch and thoracic configurations, respectively. The aggregate TV estimation bias for the patch IP was 0.008 L, whereas the thoracic IP slightly underestimated volume with an ME of −0.019 L.

During ambulation, we observed noteworthy motion artifacts in both IP configurations: exemplative signals from the patch IP during both active measurements are depicted in Fig. 5. The illustrative signals were taken from the subject with the median R^2 (Subject 6, R^2=0.911) to accurately demonstrate representative noise observed in a typical subject's data and the preservation of the relevant respiratory features after the prescribed filtering.

The r values of IP-estimated TV, found in Table 2, for all subjects and measurements were 0.934±0.046 and 0.951±0.052 for the patch and thoracic configurations. The patch IP and thoracic IP exhibited aggregated RMSEs of 0.177±0.061 L and 0.129±0.060 L, respectively. The cumulative MAPE values were 14.94±6.059% and 12.90±10.08% for the patch IP and thoracic IP, respectively. The standard deviations (SD) were relatively similar for the r and RMSE values for both configurations, however, the MAPE values showed a distinct contrast between the patch IP (SD=6.059%) and thoracic IP (SD= 10.08%). The differences in reported RMSEs were statistically significant (p=0.0151), whereas the MAPE differences were not (p=0.3783). Though RMSEs are largely influenced by the range of values measured, which differed by a mean-absolute-difference of 0.508 L between corresponding measurements, the MAPE accounts more for variations in TV, and therefore demonstrates the comparable performance between the two methods.

Statistically significant differences in the patch and thoracic IP slope coefficients were observed for each of the activities (all four p values <0.0053), whereas the y-intercept differences were not significant for any of the measurements (all four p values >0.1733). These results are expected, as the two IP configurations capture varied portions of the thoracic cavity, producing different signal amplitudes and being distinctly impacted by motion and other artifacts. The longitudinal calibration analysis demonstrated an overall increase in TV MAPE of 3.688±5.110% when applying the earlier CCs on the follow-up data as compared to estimation with CCs produced by the follow-up calibration set.

B. Estimating Respiratory Timings

The RR estimations are detailed in similar fashion to the TV results, incorporating Bland-Altman plots, Fig. 6, to contrast the errors between the two tested electrode configurations. The 12 brpm and 24 brpm breathing rates that were enforced in the static and active experiments, respectively, resulted in RRs ranging from 10.5 to 26 brpm. The limits of agreement were stricter for the static trials, 0.324 and 0.383 brpm, than in the active with 0.890 and 0.602 brpm for patch IP and thoracic IP, respectively. A RR ME of 0.021 brpm and 0.030 brpm were observed for the patch and thoracic configurations, respectively. The MAE was 0.119±0.090 brpm for the thoracic IP and 0.165±0.170 brpm for the patch IP, with MAPEs of less than 1%. The increase in MAE from the static to ambulatory measurements was due more to the increased RR rather than the added motion, as the MAPEs actually decreased relative to the static measurements—in all cases except stair-stepping with patch IP where it performed similarly.

The respiratory phase timings, INT and EXT, were estimated with cumulative MAPEs of 5.953% and 5.986%, respectively, for the patch IP. Likewise, the thoracic configuration reported MAPEs of 4.404% and 4.256% for INT and EXT, respectively. Biases of less than 0.034 s were observed for all phase timing parameters. This indicates that IP can estimate INT and EXT with almost equal precision, and the low SD (<2.7%) across all measurements and for both configurations suggests that, as with RR, the estimation accuracy of respiratory timings is not heavily impacted by the influence of activity.

IV. Discussion

This paper represents a comprehensive assessment of the feasibility of multi-frequency IP to estimate TV and respiratory timings in static and ambulatory settings. We introduced a novel, chest-based electrode configuration that offers a substantially smaller footprint to enable more convenient IP measurements while achieving comparable estimation accuracy to traditional configurations. Our multi-frequency IP system was capable of robustly estimating TV, RR, INT, and EXT—all with wide dynamic ranges—across routine postures and activities. Thus, these results promote further investigation into this promising approach for noninvasively detecting clinically relevant respiratory biomarkers during ambulation.

A. Wearable IP can Robustly Track TV and RR During Ambulation

We demonstrated, for the first time, that wearable IP can accurately estimate both TV and respiratory timings in ambulatory persons. Both the patch and thoracic configurations, the latter of which previous work had speculated might not be suitable for active conditions [36], produced precise TV and RR estimations across all measurements, but most notably during the walking and stair-stepping exercises. Despite the additional noise induced by the distinct artifact signatures, as shown in the results section, we achieved robust estimation with strong correlation and reasonable error (r=0.915, RMSE=0.195 L). The patch IP and thoracic IP's aggregate correlations—r=0.934 and r=0.951, respectively—to the reference SP signal were higher than that of previous works utilizing small form factor IP configurations that were only tested in static conditions [17], [19], signifying the high quality of the signals obtained by our custom hardware. These ambulatory results are

especially promising when factoring in the reduced calibration requirements employed in this study, considering that most IP studies do not include specific information regarding the implemented calibration methodology. With more extensive calibration, TV estimation performance would undoubtedly improve, if so desired. Concerning RR estimations, the reported accuracy of < 1% average MAPE for both configurations was consistent with—if not superior to—previous findings with wearable IP systems or with IP deployed in active settings, [17], [19], [23], [24]. This fact further highlights the capability of the proposed system to extract meaningful timing and volume parameters simultaneously with state-of-the-art precision. These four tested scenarios—sitting, supine, walking, and stair-stepping—illustrate by natural extension the feasibility of IP as a method for robustly extracting respiratory parameters throughout clinical settings and activities of daily living.

B. Novel Electrode Configuration Enhances Convenience

Overall, the TV and respiratory timing estimation results were comparable between the two different electrode configurations, with discrepancies typically explained by measurement or processing error rather than underlying deficiencies inherent to the configurations themselves. Specifically, the novel patch configuration exhibited high correlation to the ground truth SP-derived volume signal, with only slightly higher estimated TV RMSE (patch IP, RMSE=0.177 L) than the thoracic configuration (thoracic IP, RMSE=0.129 L), across all the testing environments. The patch featured significantly lower SD for TV MAPE, demonstrating consistent performance regardless of demographic factors, such as sex or weight, in this population. A difference of only 0.207% existed across the average estimated RR MAPEs between the configurations—the patch IP having the higher error—with both values showing less than 1% error relative to the ground truth. The patch was even found—if excluding Subject 3's data that was responsible for most substantial RR errors—to estimate RR more accurately with an MAE of 0.121 brpm compared to the 0.125 brpm MAE of the thoracic configuration.

Subject-specific results for both IP configurations consistently exhibited strong R^2 values to the reference SP signal. Subject 10 had the weakest correlation among all the subjects (R^2=0.743) for patch IP, which was due primarily to the divergent baseline breathing periods in several of the measurements that seemingly necessitated a different linear fit than the shallow and deep breathing periods indicated. This observation was consistent with the subject's thoracic IP data as well, so the controlled breathing tasks likely induced irregular breathing mechanics, affecting the linearity.

The comparative results in Table 2 highlight the surprisingly small tradeoff between form factor and estimation accuracy; thoracic IP is generally more correlated to lung volume due to current paths traversing the entirety of the thorax, while the patch IP is limited by the small inter-electrode distances but is still strongly correlated with respiratory function. The proposed patch configuration, with a marginal penalty for adopting a significantly more convenient form factor, represents a considerable step towards ubiquitous IP-based respiratory monitoring in clinical or at-home settings.

C. Respiratory Phase Timings can be Accurately Extracted from IP

The breath onsets, detected to extract TV from a volume signal, can be utilized for more than just TV and RR estimations. Particularly, prior work has shown this usefulness of IP for extracting timing parameters beyond RR, such as evaluating the ratio of the peak tidal expiratory flow and expiratory time [37]; however, the fidelity of IP extracted INT and EXT have never been independently assessed. Our work has demonstrated that both phase timings can be reasonably quantified from the patch IP volume signal, with less than 6% aggregated MAPE from the reference SP timings. In addition, the aforementioned study [37] only included measurements limited to the sitting posture, however, the expansive active scenarios examined in this work point towards feasible ambulatory detection of timing parameters, as accuracy was not markedly hindered by motion artifacts. By providing breath-by-breath extracted phase timings, subjects with elongated expiration [5] or inspiration times [4] can be readily identified, aiding in clinical diagnosis.

D. Multi-Frequency IP Aids with Inter-Subject Variability

Across the four examined frequencies (5 kHz, 50 kHz, 100 kHz, 150 kHz), the average results were comparable, as seen in Table 1, but are not entirely indicative of the subject-specific efficacy. Specifically, the SQI identified quality segments, those expected to produce reliable features, for analysis which led to acceptable estimation performance. Thus, analogous results across all frequencies were observed. However, upon investigating the rejected segments based on the SQI, a considerable 11% of all 30-second segments were not uniform across all frequencies, i.e., at some measured IP frequencies a segment was deemed acceptable while for other frequencies the same segment was removed. This incongruity bolsters the case for including multiple frequency measurements, as single-frequency systems are limited if the lone IP signal is distorted by noise or other external factors.

Multi-frequency IP was especially beneficial for the patch configuration, with its short electrode distances placing greater importance on the current path and penetration depth dictated by the excitation frequency. For example, Subject 3, a male subject with body hair that interfered with the patch electrode placement, is emblematic of the potential consequences when single-frequency IP systems. The poor affixation resulted in highly variable performance between measured frequencies in the different postures and activities. Dependency on any individual frequency for this subject would result in discarding significant segments of data—if not entire measurements—that were, for other frequencies, regarded as high quality by the SQI. Thus, the reported estimation performance would likely improve if a given segment’s features were selected from the IP frequency with the highest SQI, rather than from a single frequency throughout. This reveals the practicality and, in some cases, necessity of utilizing additional IP frequencies, especially if a noninvasive chest-based system is desired.

Another advantage of employing multi-frequency IP is the potential for a synthesized respiratory estimation approach, where, in the instances with multiple serviceable IP frequencies, estimated parameters can be cross validated between the measured frequencies. This technique would prove especially relevant in clinical settings, where false positives,

potentially from reporting too high or too low TV or RR, waste resources and can affect the diagnoses of patients [8]. Furthermore, implementation of an automated frequency selection algorithm to extract features from a segment based on the IP frequency with the highest SQI would be another safeguard for ensuring only high-fidelity features are obtained. The use of multiple frequencies could also lead to advances in calibration, either via simplification or implementation of globalized models, or assist in the extrication of the respiratory signal from motion artifacts, as discussed later.

E. Limitations and Future Work

1) Uncontrolled Experimental Settings and Subjects with Cardiopulmonary Disorders—The approach proposed in this work, including both the novel patch configuration and multi-frequency IP system, requires further validation in more diverse subject populations, particularly among high BMI persons, without a contrived breathing protocol to assess if natural breathing parameters can be accurately detected. The TV estimation needs to be validated in uncontrolled settings, where TV and RR will naturally vary from the parameters in the calibration set, granting insight into the potential bounds and limitations of the IP amplitude and TV linearity, if any.

Additionally, based on our findings, noninvasive wearable IP should be employed in dynamic settings such as at-home monitoring sessions or cardiopulmonary exercise testing, situations where IP has yet to show promise. IP's effectiveness in such conditions could elucidate the clinical utility of respiratory monitoring and determine if IP can fill the void of noninvasive TV monitoring methods. Finally, clinical studies involving patients with cardiorespiratory disorders would serve as a proper indication of the ultimate efficacy of wearable IP for identifying pulmonary deterioration in affected populations.

2) Wearable Hardware Development—To best utilize the patch electrode configuration for wearable IP, the current hardware—that was adapted from other applications—needs to be redesigned for optimal respiratory sensing by including only relevant sensors and adopting a smaller package. The proximity of the proposed electrode configuration to regions already ubiquitous in cardiac sensing lends itself for integration into a multi-modal system capable of capturing a variety of physiological parameters, as in [38]. Incorporating our group's previously developed multi-modal wearable patch, capable of measuring electrocardiogram (ECG) and seismocardiogram (SCG) signals [39], with the 5.1 cm × 5.1 cm electrode configuration and AD5940 EBI front-end would enable a more holistic assessment of cardiopulmonary health.

With the demonstrated 16 Hz sampling rate proving more than sufficient for capturing pertinent respiratory information, real-time wearable respiratory monitoring via IP is now becoming increasingly viable. Even with limited storage capacity and on-chip processing capabilities, TV, RR, and phase timings could feasibly be extracted in real-time on a wearable system with lightweight preprocessing. The implementation of wireless modules to offload data processing and analysis is another practical approach for especially constrained systems.

3) Calibration and Artifact Removal—Due to the stringent state of IP calibration methodology, there is a need to improve the generalization of IP and reduce the burden of calibration. The current posture-dependent calibration would require—for use in practical scenarios—IP and spirometer data to be collected from several archetypal postures, i.e., sitting, supine, to produce multiple regression fits that would account for most free-living conditions. Inevitably, subjects would adopt positions that vary from the archetypal postures and incur reduced TV estimation accuracy, but generally the set of CCs would allow for similar performance across the common postures. This methodology would also require knowledge of the subject's posture to determine which CCs to employ, which is feasible with the integrated accelerometers or even IP itself [40]. Though we demonstrated the persistence of the calibration, it is an onerous task for subjects.

However, there are several promising approaches to improve upon this inconvenient methodology. As we observed that several of the subjects had very similar regression lines for all postures, shown in Fig. 4(a), uncovering the transfer function between these calibration lines via the fusion of accelerometry and IP could lead to generalizing a single regression for all postures. As changes in posture alter the geometry of the thoracic cavity, the low-frequency acceleration due to breathing detected by a chest-mounted accelerometer will correspondingly change [41]. Coupling this with the posture-induced changes in IP, these natural changes in posture from daily living could potentially be compensated for in the estimation of TV. Additionally, the introduction of dual-frequency calibration, as detailed in recent work [29], displays promising efforts to reduce posture and subject-specific calibration. Posture-induced changes in IP propagate consistently across the measured frequencies, allowing for subject-specific alterations in IP to be mitigated by utilizing the ratio of low to high frequency IP.

Similar methods could be employed to address otherwise unusable data tainted by motion artifacts, supposing that they proportionally affect each frequency. As the higher measured frequencies—50 kHz and above—were observed in our work to be markedly congruous, due to similar excitation current paths, it seems forthright to employ algorithms that exploit the distinctive properties of the 5 kHz IP signal in conjunction with the kindred higher frequencies. Such algorithms can utilize the diverse information provided to concurrently eradicate noise common across frequencies and enrich the respiratory features. A better understanding of how respiration modulates these extra and intra-cellular current paths differently could be crucial for employing these unique frequencies in a meaningful fashion. Along with multi-frequency analysis, the often-neglected reactive component of impedance should be further explored to identify whether it has relevancy for detecting respiratory function or the removal of artifacts. Finally, input from complementary sensors such as accelerometers, can also inform the artifact removal processes, as changes in posture or movement can be anticipated and corrected [20].

V. Conclusion

Noninvasive ambulatory respiratory monitoring facilitates remote patient surveillance, providing clinicians with vital indications of respiratory decline without impractical and intrusive mask-based devices. We have demonstrated that wearable multi-frequency IP

paired with a small chest-worn form factor can detect pertinent respiratory parameters, including TV, RR, INT, and EXT, on a breath-by-breath basis. With accuracy comparable to conventional, but unwieldy, electrode configurations, this novel patch-based configuration enables robust and convenient IP measurements. Validated in both static and active settings, IP displayed its potential for ambulatory respiratory monitoring, which could be utilized for patients with respiratory diseases such as HF or COPD to quantify loss of pulmonary function. The presented IP methodology could also be employed to manage quality of life for people suffering from chronic, debilitating conditions such as asthma or sleep apnea. Supplementing this work with extended, at home and in-clinic studies—on a more diverse population—would further validate the robustness of IP as a lung volume surrogate and assess its clinical relevancy for monitoring cardiopulmonary illnesses.

Acknowledgments

This work was supported by the National Science Foundation / National Institutes of Health Smart and Connected Health Program under Grant 1R01EB023808.

References

[1]. Agostoni P et al. “Cardiopulmonary interaction in heart failure,” Pulm. Pharmacol. Ther, vol. 20, no. 2, pp. 130–134, Apr. 2007, doi: 10.1016/J.PUPT.2006.03.001. [PubMed: 16702004]

[2]. Apostolo A et al. “Lungs in heart failure,” Pulm. Med, 2012, doi: 10.1155/2012/952741.

[3]. O’Donnell DE and Laveneziana P, “The clinical importance of dynamic lung hyperinflation in COPD,” COPD J. Chronic Obstr. Pulm. Dis, vol. 3, no. 4, pp. 219–232, 2006, doi: 10.1080/15412550600977478.

[4]. Mooney AM et al. “Relative prolongation of inspiratory time predicts high versus low resistance categorization of hypopneas,” J. Clin. Sleep Med, vol. 8, no. 2, pp. 177–185, 2012, doi: 10.5664/jcsm.1774. [PubMed: 22505863]

[5]. Gazi AH et al. “Transcutaneous Cervical Vagus Nerve Stimulation Lengthens Exhalation in the Context of Traumatic Stress,” IEEE Biomed. Heal. Informatics Conf. 2021.

[6]. Massaroni C et al. “Remote Respiratory Monitoring in the Time of COVID-19,” Front. Physiol, vol. 11, no. May, pp. 1–4, 2020, doi: 10.3389/fphys.2020.00635. [PubMed: 32038307]

[7]. Vanegas E et al. “Sensing systems for respiration monitoring: A technical systematic review,” Sensors (Switzerland), vol. 20, no. 18, pp. 1–84,2020, doi: 10.3390/s20185446.

[8]. Folke M et al. “Critical review of non-invasive respiratory monitoring in medical care,” Med. Biol. Eng. Comput, vol. 41, no. 4, pp. 377–383, 2003, doi: 10.1007/BF02348078. [PubMed: 12892358]

[9]. Rolfe S, “The importance of respiratory rate monitoring,” Br. Jounral Nurs, vol. 28, no. April, pp. 504–508, 2019.

[10]. Elliott M, “Why is Respiratory Rate the Neglected Vital Sign? A Narrative Review,” Int. Arch. Nurs. Heal. Care, vol. 2, no. 3, 2016, doi: 10.23937/2469-5823/1510050.

[11]. Askanazi J et al. “Effects of respiratory apparatus on breathing pattern,” 10.1152/jappl.1980.48.4.577, vol. 48, no. 4, pp. 577–580, 1980, doi: 10.1152/JAPPL.1980.48.4.577.

[12]. Ernst JM et al. “Impedance pneumography: Noise as signal in impedance cardiography,” Psychophysiology, vol. 36, no. 3, pp. 333–338, 1999, doi: 10.1017/S0048577299981003. [PubMed: 10352556]

[13]. Seppä VP et al. “Assessment of pulmonary flow using impedance pneumography,” IEEE Trans. Biomed. Eng, vol. 57, no. 9, pp. 2277–2285, 2010, doi: 10.1109/TBME.2010.2051668. [PubMed: 20542759]

[14]. Seppä VP et al. “Novel electrode configuration for highly linear impedance pneumography,” Biomed. Tech, vol. 58, no. 1, pp. 35–38, 2013, doi: 10.1515/bmt-2012-0068.

[15]. Sahakian AV et al. “Electrode Motion Artifacts in Electrical Impedance Pneumography,” IEEE Trans. Biomed. Eng, vol. BME-32, no. 6, pp. 448–451, 1985, doi: 10.1109/TBME.1985.325453.

[16]. Vuorela T et al. “Design and implementation of a portable long-term physiological signal recorder,” IEEE Trans. Inf. Technol. Biomed, vol. 14, no. 3, pp. 718–725, May 2010, doi: 10.1109/TITB.2010.2042606. [PubMed: 20172837]

[17]. Klum M et al. “Wearable Impedance Pneumography,” Curr. Dir. Biomed. Eng, vol. 6, no. 3, pp. 0–3, 2020, doi: 10.1515/cdbme-2020-3059.

[18]. Jeyhani V et al. “Optimal short distance electrode locations for impedance pneumography measurement from the frontal thoracic area,” IFMBE Proc, vol. 57, pp. 1138–1143, 2016, doi: 10.1007/978-3-319-32703-7_223.

[19]. Klum M et al. “Short distance impedance pneumography,” Curr. Dir. Biomed. Eng, vol. 4, no. 1, pp. 109–113, 2018, doi: 10.1515/cdbme-2018-0028.

[20]. Ansari S et al. “Motion Artifact Suppression in Impedance Pneumography Signal for Portable Monitoring of Respiration: An Adaptive Approach,” IEEE J. Biomed. Heal. Informatics, vol. 21, no. 2, pp. 387–398, 2017, doi: 10.1109/JBHI.2016.2524646.

[21]. Khambete ND et al. “Movement Artefact Rejection in Impedance Pneumography,” Physiol. Meas, vol. 21, no. 1, pp. 79–88, 2000, doi: 10.1088/0967-3334/21/1/310. [PubMed: 10720002]

[22]. Lahtinen O et al. “Optimal electrode configurations for impedance pneumography during sports activities,” IFMBE Proc, vol. 22, pp. 1750–1753, 2008, doi: 10.1007/978-3-540-89208-3_417.

[23]. Jeyhani V et al. “Comparison of simple algorithms for estimating respiration rate from electrical impedance pneumography signals in wearable devices,” Health Technol. (Berl)., vol. 7, no. 1, pp. 21–31, 2017, doi: 10.1007/s12553-016-0156-0.

[24]. Seppä VP et al. “Measuring respirational parameters with a wearable bioimpedance device,” IFMBE Proc, vol. 17 IFMBE, no. January, pp. 663–666, 2007, doi: 10.1007/978-3-540-73841-1_171.

[25]. Seppä VP et al. “Assessment of breathing parameters during running with a wearable bioimpedance device,” IFMBE Proc, vol. 22, pp. 1088–1091,2008, doi: 10.1007/978-3-540-89208-3_260.

[26]. Malhotra R et al. “Cardiopulmonary Exercise Testing in Heart Failure,” JACC Hear. Fail, vol. 4, no. 8, pp. 607–616, 2016, doi: 10.1016/j.jchf.2016.03.022.

[27]. Ganju AA et al. “Cardiopulmonary exercise testing in evaluation of patients of chronic obstructive pulmonary disease.,” Indian J. Chest Dis. Allied Sci, vol. 53, no. 2, pp. 87–91, 2011. [PubMed: 21545069]

[28]. Teague CN et al. “A Wearable, Multimodal Sensing System to Monitor Knee Joint Health,” IEEE Sens. J, vol. 20, no. 18, pp. 10323–10334, 2020, doi: 10.1109/JSEN.2020.2994552.

[29]. Jung H et al. “Impedance Pneumography: Assessment of Dual-Frequency Calibration Approaches,” IEEE-EMBS Int. Conf. Wearable Implant. Body Sens. Networks (BSN), Virtual, 2021.

[30]. Medical Electrical Equipment – Part 1-11: General Requirements for Basic Safety and Essential Performance – Collateral Standard: Requirements for medical electrical Equipment and Medical Electrical Systems Used in the Home Healthcare Environment. 2015.

[31]. Mabrouk S et al. “Robust Longitudinal Ankle Edema Assessment Using Wearable Bioimpedance Spectroscopy,” IEEE Trans. Biomed. Eng, vol. 67, no. 4, pp. 1019–1029, 2020, doi: 10.1109/TBME.2019.2927807. [PubMed: 31295102]

[32]. Rosell J and Webster JG, “Signal-to-Motion Artifact Ratio Versus Frequency for Impedance Pneumography,” IEEE Trans. Biomed. Eng, vol. 42, no. 3, pp. 321–323, 1995, doi: 10.1109/10.364521. [PubMed: 7698789]

[33]. Nevius B, “The mechanical design and optimization of a wearable multimodal health sensing system,” 2020.

[34]. Charlton PH et al. “An impedance pneumography signal quality index: Design, assessment and application to respiratory rate monitoring,” Biomed. Signal Process. Control, vol. 65, no. September 2020, p. 102339, 2021, doi: 10.1016/j.bspc.2020.102339. [PubMed: 34168684]

[35]. Seppi VP et al. “Measuring respirational parameters with a wearable bioimpedance device,” IFMBE Proc, vol. 17 IFMBE, no. January, pp. 663–666, 2007, doi: 10.1007/978-3-540-73841-1_171.

[36]. Młyńczak M et al. “Assessment of calibration methods on impedance pneumography accuracy,” Biomed. Tech, vol. 2015, no. 6, pp. 587–593, 2015, doi: 10.1515/bmt-2015-0125.

[37]. Seppä VP et al. “A method for suppressing cardiogenic oscillations in impedance pneumography,” Physiol. Meas, vol. 32, no. 3, pp. 337–345, 2011, doi: 10.1088/0967-3334/32/3/005. [PubMed: 21321385]

[38]. Klum M et al. “Wearable Multimodal Stethoscope Patch for Wireless Biosignal Acquisition and Long-Term Auscultation,” Proc. Annu. Int. Conf. IEEE Eng. Med. Biol. Soc. EMBS, pp. 5781–5785, 2019, doi: 10.1109/EMBC.2019.8857210.

[39]. Shandhi MMH et al. “Wearable Patch-Based Estimation of Oxygen Uptake and Assessment of Clinical Status during Cardiopulmonary Exercise Testing in Patients With Heart Failure,” J. Card. Fail, vol. 26, no. 11, pp. 948–958, 2020, doi: 10.1016/j.cardfail.2020.05.014. [PubMed: 32473379]

[40]. Dutt AG et al. “Wearable bioimpedance for continuous and context-aware clinical monitoring,” Proc. Annu. Int. Conf. IEEE Eng. Med. Biol. Soc. EMBS, vol. 2020-July, pp. 3985–3988, Jul. 2020, doi: 10.1109/EMBC44109.2020.9175298.

[41]. DH P et al. “Estimation of respiratory waveform and heart rate using an accelerometer,” Annu. Int. Conf. IEEE Eng. Med. Biol. Soc. IEEE Eng. Med. Biol. Soc. Annu. Int. Conf, vol. 2008, pp. 4916–4919, 2008, doi: 10.1109/IEMBS.2008.4650316.

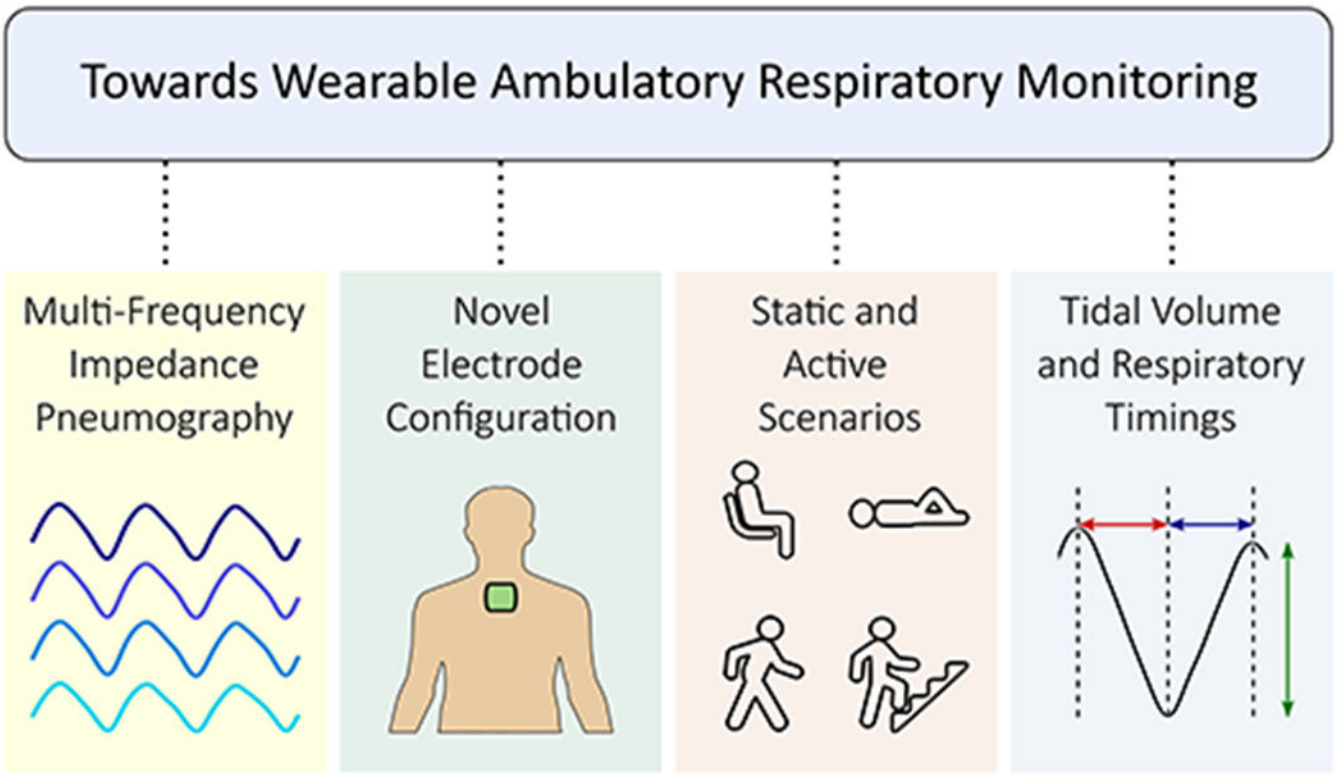

Fig. 1. High-level overview of this work.

Multi-frequency impedance pneumography (IP) was employed to extract respiratory parameters such as tidal volume (TV), respiration rate (RR), inspiratory time (INT), and expiratory time (EXT). A broad range of IP frequencies were used to ensure viability across subject populations and in the presence of motion artifacts, which were observed during conventional static postures and previously untested ambulatory experiments. A novel electrode configuration was presented as a convenient alternative to obtrusive transthoracic configurations and can be utilized to enable wearable respiratory monitoring in ambulatory settings.

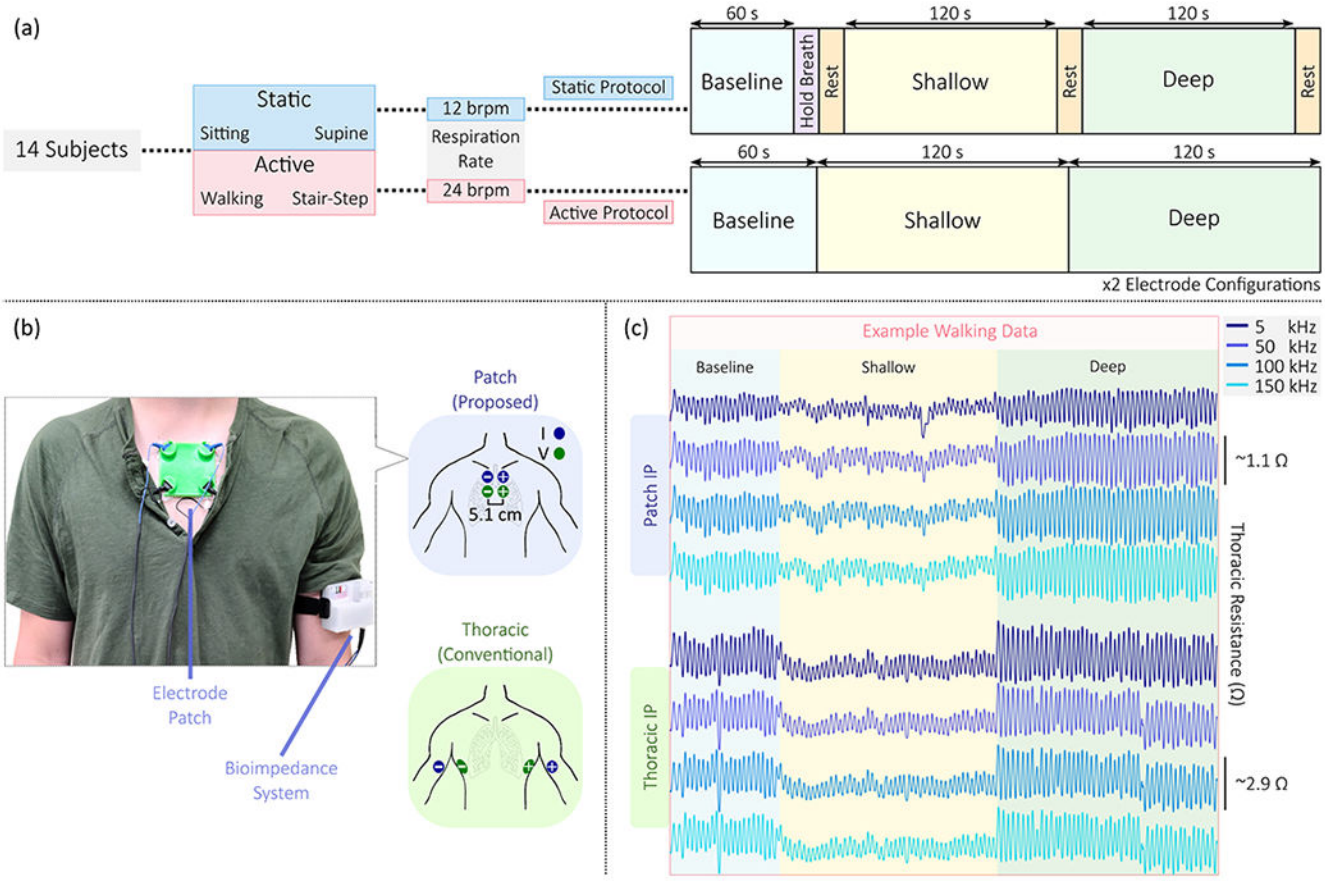

Fig. 2. Protocol diagram with exemplative data.

(a) 14 subjects underwent four separate measurements where impedance pneumography (IP) and concurrent spirometry (SP) were captured for two electrode configurations. Measurements were taken while sitting, lying supine, walking and stair-stepping for up to 6 minutes, with specified respiratory rates (RRs) displayed, and included distinct periods of breath-volume modulation. **(b)** The electrode positionings of the two tested configurations are depicted, with an image of the 3D-printed patch and bioimpedance system on a subject shown for reference. **(c)** Example impedance pneumography (IP) data from walking measurements are shown for the patch and thoracic configurations, with all four measured frequencies presented.

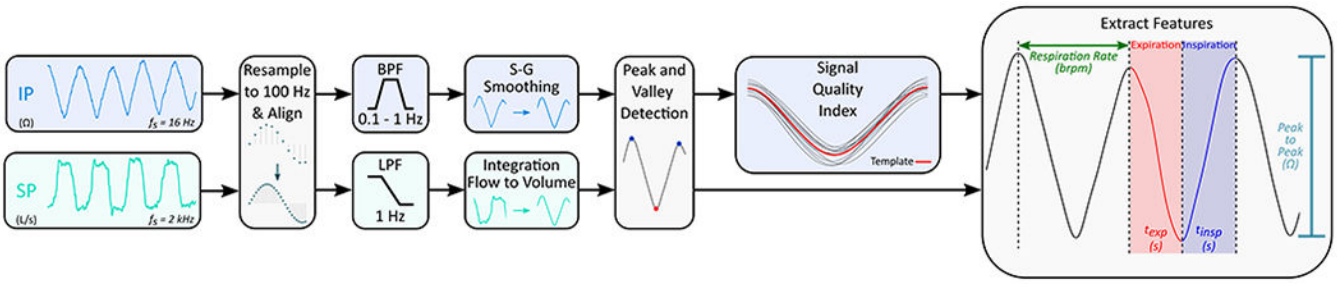

Fig. 3. Signal processing pipeline for the respiratory signals.

The spirometer (SP) and multi-frequency impedance pneumography (IP) signals are resampled and aligned for synchronization. The IP signal is bandpass filtered and conditioned with Savitzky-Golay (S-G) smoothing with a 1000 ms frame. The SP airflow signal is lowpass filtered and integrated from the inspiration onsets to form the ground truth volume signal. The peaks and valleys of all signals are detected for 30-second segments, and a signal quality index (SQI) is employed for the IP signal to remove poor segments prior to the extraction of respiratory features.

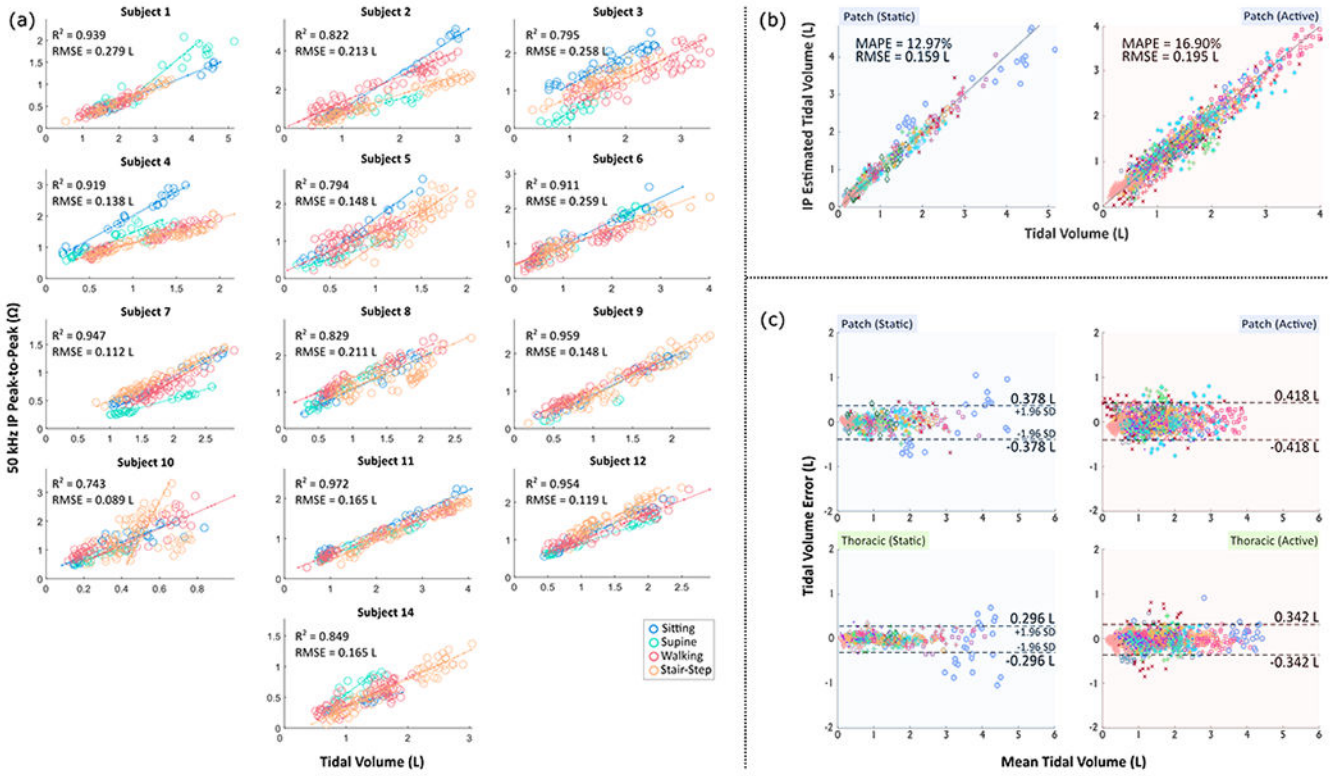

Fig. 4. Tidal volume estimation results.

(a) Correlation plots for each subject, with each individual measurement denoted, are shown between patch impedance pneumography (IP) peak-to-peak values ground truth spirometer-based tidal volume (TV). The regression lines for each measurement are shown, and the resulting average coefficient of determination (R^2) and root-mean-square-error (RMSE) for the estimated TV values are presented for each subject. **(b)** The cumulative correlation plots for the patch configuration's impedance pneumography (IP) estimated tidal volume (TV) versus gold-standard spirometer TV are depicted for the static (left, shaded-blue) and active (right, shaded-right) scenarios. The mean-absolute-percent-error (MAPE) and root-mean-square-error (RMSE) were aggregated across all subjects and are reported. **(c)** Bland-Altman plots demonstrating the relationship between the impedance pneumography (IP) estimated tidal volume (TV) and the reference spirometer-based TV. Static and active measurements results are displayed for both configurations.

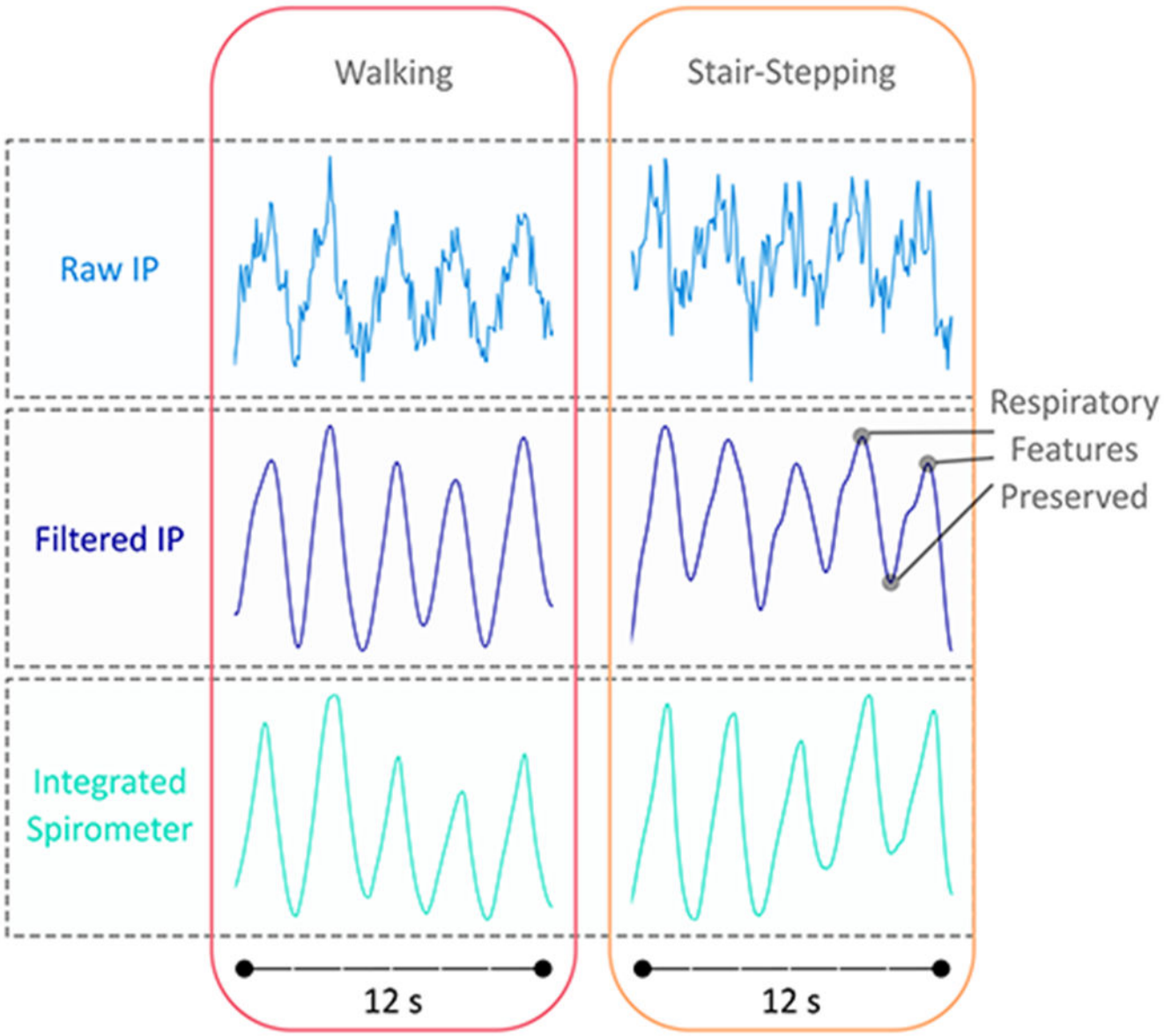

Fig. 5. Representative motion artifacts during activity.

Impedance pneumography (IP) signals, measured with the patch electrode configuration during the walking and stair-stepping exercises, are shown before and after filtering to illustrate the retention of respiratory information. The corresponding spirometer volume signal is depicted below for reference.

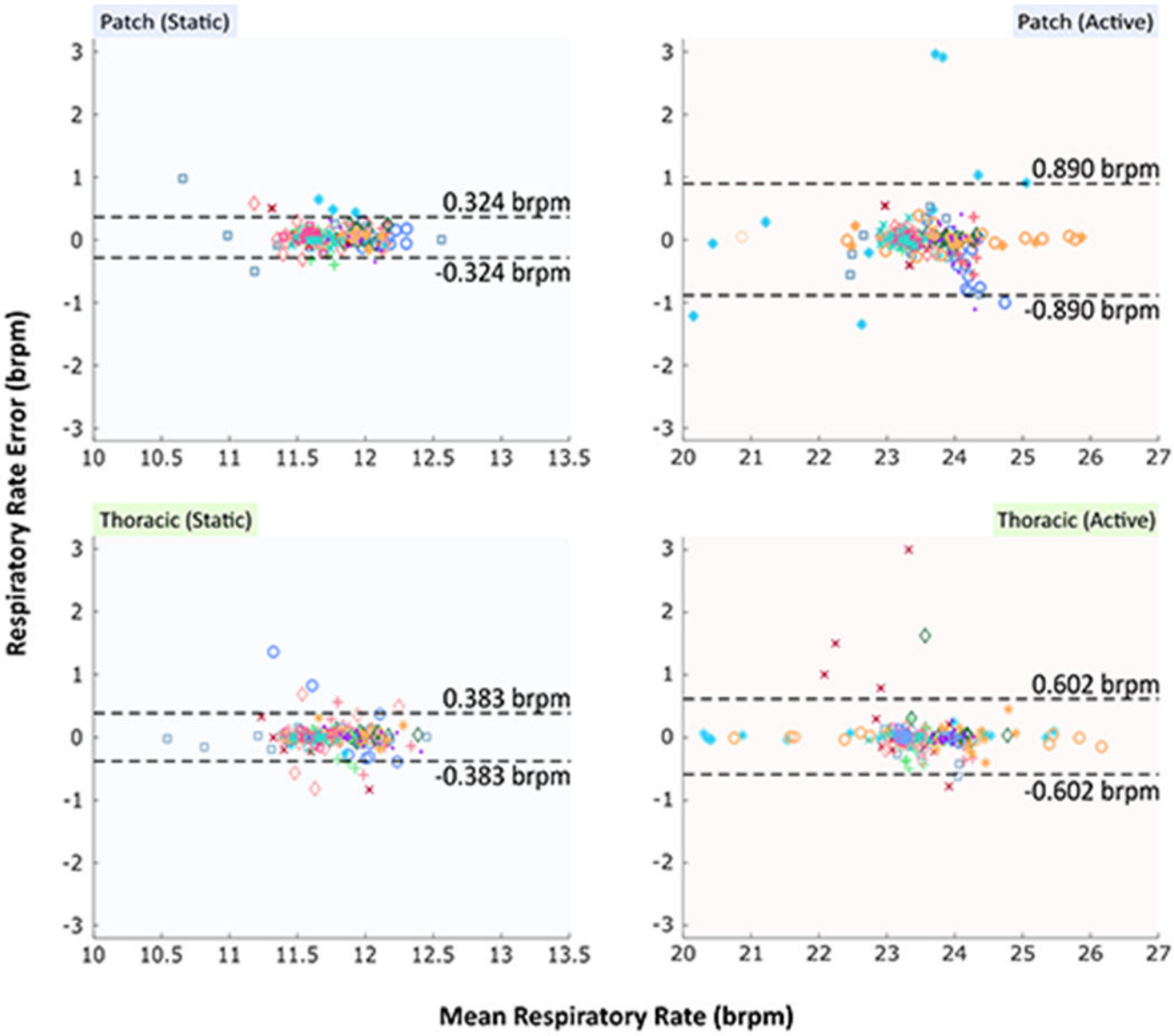

Fig. 6. Bland-Altman plots for respiration rate.

Bland-Altman plots with impedance pneuomgraphy (IP) estimated respiration rate (RR) and ground truth spirometer-based RR are presented. The static (left, shaded blue) and active (right, shaded red) results are explicitly shown for both the patch and thoracic electrode configurations.

Table 1

Aggregate Multi-Frequency Impedance Pneumography Results

Config	Frequency (kHz)	Correlation r_{vol}	TV $RMSE_L$	TV $MAPE_{\%}$	Quality $Segments_{\%}$
Thorax	5	0.950 ± 0.054	0.141 ± 0.073	14.09 ± 12.33	95.58 ± 5.016
	50	0.954 ± 0.052	0.125 ± 0.063	12.93 ± 11.29	96.15 ± 3.902
	100	**0.951 ± 0.052**	**0.129 ± 0.060**	**12.90 ± 10.08**	**96.35 ± 3.766**
	150	0.948 ± 0.059	0.140 ± 0.093	14.16 ± 12.26	95.96 ± 4.952
Patch	5	0.923 ± 0.049	0.187 ± 0.073	14.24 ± 4.712	87.88 ± 9.940
	50	**0.934 ± 0.046**	**0.177 ± 0.061**	**14.94 ± 6.059**	**90.38 ± 8.026**
	100	0.912 ± 0.093	0.189 ± 0.090	15.09 ± 6.852	88.08 ± 10.61
	150	0.881 ± 0.180	0.204 ± 0.093	16.21 ± 6.222	88.85 ± 11.44

All values reported are of the form mean±standard deviation (SD).

Table 2

Respiratory Parameter Estimation Results

Pose/Activity	Config	Correlation r_{vol}	TV $RMSE_L$	TV $MAPE_{\%}$	RR MAE_{bpm}	RR $MAPE_{\%}$	INT $MAPE_{\%}$	EXT $MAPE_{\%}$
Sitting	Thorax	0.980 ± 0.043	0.087 ± 0.054	11.94 ± 19.14	0.107 ± 0.137	0.905 ± 1.148	4.454 ± 4.334	4.739 ± 3.686
	Patch	0.976 ± 0.021	0.146 ± 0.054	12.47 ± 5.086	0.112 ± 0.058	0.955 ± 0.510	3.814 ± 3.283	4.322 ± 3.732
Supine	Thorax	0.949 ± 0.128	0.113 ± 0.132	12.04 ± 9.793	0.106 ± 0.076	0.901 ± 0.640	4.794 ± 4.335	4.797 ± 3.127
	Patch	0.928 ± 0.099	0.172 ± 0.146	13.48 ± 6.742	0.116 ± 0.072	0.977 ± 0.594	7.359 ± 7.468	6.284 ± 4.228
Walking	Thorax	0.962 ± 0.032	0.144 ± 0.094	13.95 ± 13.08	0.115 ± 0.120	0.489 ± 0.517	4.245 ± 3.205	3.740 ± 2.013
	Patch	0.929 ± 0.071	0.197 ± 0.091	19.82 ± 13.83	0.177 ± 0.148	0.771 ± 0.689	4.691 ± 3.150	4.939 ± 3.142
Stair-Step	Thorax	0.912 ± 0.124	0.173 ± 0.100	13.68 ± 13.29	0.149 ± 0.196	0.622 ± 0.820	4.124 ± 1.728	3.750 ± 1.474
	Patch	0.901 ± 0.128	0.194 ± 0.076	13.98 ± 7.697	0.254 ± 0.442	1.039 ± 1.749	7.946 ± 4.142	8.398 ± 5.246
Total	**Thorax**	**0.951 ± 0.052**	**0.129 ± 0.060**	**12.90 ± 10.08**	**0.119 ± 0.090**	**0.729 ± 0.508**	**4.404 ± 2.631**	**4.256 ± 2.050**
	Patch	**0.934 ± 0.046**	**0.177 ± 0.061**	**14.94 ± 6.059**	**0.165 ± 0.170**	**0.936 ± 0.815**	**5.953 ± 2.668**	**5.986 ± 2.309**

All values reported are of the form mean±standard deviation (SD).

IEEE Trans Biomed Eng. Author manuscript; available in PMC 2023 June 01.